International Journal of Hydrogen Energy 180 (2025) 151741

Contents lists available at ScienceDirect

International Journal of Hydrogen Energy

journal homepage: www.elsevier.com/locate/he

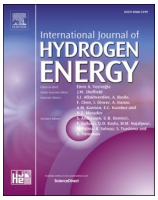

Analysis of the influence of hydrogen on prismatic loops and dislocation dipole structure in an austenitic steel: Effect on stacking fault energy

Ivan Gutierrez-Urrutia *, Yuhei Ogawa, Akinobu Shibata

Research Center for Structural Materials, National Institute for Materials Science (NIMS), 1-2-1, Sengen, Tsukuba 305-0047, Japan

ARTICLE INFO

Keywords:
Austenitic steel
Hydrogen
Dislocation dipoles
Stacking fault energy

ABSTRACT

The influence of hydrogen on crystal defects (point defects and dislocations) determines effects such as hydrogen-induced localized plasticity and damage. One of the structural variables controlling these effects is the stacking fault energy. Experimental and computational studies indicate that hydrogen reduces its value, thereby increasing the partial dislocation spacing, and influencing dislocation behavior. This study quantitatively investigates the influence of solute hydrogen (133 mass ppm) on prismatic loop and dislocation dipole structures in an austenitic steel by an approach based on scanning transmission electron microscopy (STEM) and anisotropic dislocation theory. The established method allows the estimation of the stacking fault energy with greater accuracy than approaches used in the literature. We show that hydrogen leads to several effects on crystal defects, increasing the average prismatic loop size and average dipole height of screw-type dipoles. The analysis of the dissociated dipole structure by a model based on anisotropic dislocation theory indicates that hydrogen reduces the stacking fault energy. We critically compare the present study with former reports in fcc materials and discuss the influence of hydrogen-charging conditions, imaging analysis method, and dislocation theory on the measurement of stacking fault energy. The effect of the present results on the deformation behavior is evaluated.

1. Introduction

In face-centered cubic (fcc) metals, crystal defects, such as dislocation dipoles, stacking faults, dislocations, and dislocation loops, and their interactions contribute to the deformation behavior. In particular, under uniaxial deformation conditions, dislocation dipoles can form stable deformation debris that contributes to dislocation exhaustion. These structures reduce the dislocation mean free path by acting as additional obstacles to the primary slip system, enhancing strain hardening [1,2]. However, few studies have examined the impact of hydrogen on dislocation loops and dislocation dipoles. Hachet et al. [3,4] have investigated the influence of hydrogen, vacancies, and vacancy clusters on the stability of dipoles in Ni during cyclic loading by atomic calculations. These studies show that hydrogen enhances the mechanical stability of edge dipoles due to a hardening effect associated with Cottrell's atmospheres of hydrogen. Interestingly, these studies also predict that the addition of hydrogen to Ni reduced the spacing of edge-type dislocation partials, increasing stacking fault energy (γ_{SFE}). This result contradicts computational calculations, predicting a hydrogen-induced reduction in γ_{SFE} of fcc materials by up to 40 % [5–9]. These studies suggest that hydrogen increases the dissociated dislocation spacing, promoting localized planar slip. In Fe–Ni–Cr austenitic steels, molecular dynamic calculations have shown that hydrogen-induced reduction in γ_{SFE} is strongly dependent on hydrogen content [9]. These calculations indicate that while a hydrogen content of 1 at. % reduces γ_{SFE} by 5–7 %, the addition of 10 at. % has a stronger effect on γ_{SFE}, decreasing its value by 53–72 %. From an experimental standpoint, hydrogen additions larger than 1 at. % in fcc materials can be only produced in micron-scale surface layers using electrochemical charging methods [10], limiting the influence of hydrogen in γ_{SFE}. Experimental studies based on transmission electron microscopy (TEM) approaches have estimated a hydrogen-induced reduction in γ_{SFE} of ~20 % in an Fe–19Ni–24Cr austenitic steel [11] and ~28 % in a Cr–Mn–Fe–Co–Ni fcc alloy [12]. However, these studies present several concerns about the methods used to estimate hydrogen content and the imaging analysis, raising doubts about the estimated γ_{SFE}. For instance, in the study by Ferreira et al. [11], the hydrogen content was not measured. In the study by Kim et al. [12], the selected hydrogen charging method (electrochemical charging) produces a strong hydrogen gradient associated with surface compressive internal stresses

* Corresponding author.
E-mail address: gutierrezurrutia.Ivan@nims.go.jp (I. Gutierrez-Urrutia).

https://doi.org/10.1016/j.ijhydene.2025.151741
Received 23 July 2025; Received in revised form 9 September 2025; Accepted 24 September 2025
Available online 30 September 2025

generated at the sample surface [10]. This effect influences the hydrogen diffusion rate, which was not considered in that study. This makes the estimated hydrogen content at the investigated sample depth questionable. Besides, these studies have analyzed their data using isotropic dislocation theory. Multicomponent fcc alloys are anisotropic materials, which influences the values of the elastic stiffness constants and Poisson's ratio used to determine the distance between partials. As shown in Ref. [13], the anisotropic dislocation theory can estimate the dissociated dislocation spacing with greater accuracy, which is essential to determine the influence of hydrogen on γ_{SFE}.

The objective of this study is to quantitatively analyze the impact of hydrogen on the prismatic loop and dislocation dipole structures of a Fe–Ni–Cr austenitic steel to understand the effect of hydrogen on these crystal defects. From this analysis, we also aim to evaluate the effect of hydrogen on structural variables, such as γ_{SFE}. This parameter controls the spacing between dislocation partials, influencing the behavior of dislocation plasticity. Statistical analyses of prismatic loop size and dipole height were performed in a tensile-deformed Fe–19Ni–24Cr (wt. %) austenitic steel uniformly charged with 133 mass ppm solute hydrogen by scanning transmission electron microscopy (STEM). This electron microscopy technique allows the imaging of dislocations and dislocation loops with enhanced contrast in highly dense dislocation configurations due to the suppression of bend contour-induced contrast and improved signal-to-noise ratio compared to conventional transmission electron microscopy (TEM) imaging modes [14,15]. Crystal defects were characterized using an imaging approach that analyzes the intensity contrast profile across crystal defects on STEM images and considers the projection geometry of the imaged defect. To evaluate the effect of hydrogen on γ_{SFE} with greater accuracy, the dissociated dipole structure was analyzed by a dislocation model based on anisotropic dislocation theory. The influence of this effect on deformation behavior is discussed. The results obtained in this study were compared with computational and experimental studies on fcc materials. Experimental and methodological differences of the present study to former experimental approaches were critically evaluated.

2. Materials and methods

The steel investigated in the present study was a commercially available Fe–19Ni–24Cr (wt. %) (Type 310S) austenitic steel with a grain size of 30 − 70 μm. The mechanical tests were conducted using a cylindrical specimen with a 6 mm diameter at an initial strain rate of 5 $\times 10^{-5}$/s in laboratory air at 295 K [16]. The hydrogen charging process was performed before the tensile tests by exposing the tensile specimens to a pressurized gaseous hydrogen environment of 100 MPa and 270 °C for 200 h in an autoclave. This charging condition was set based on our former work [17]. This study demonstrates that the selected charging conditions ensure a uniform distribution of hydrogen in the gauge part of the tensile specimens. After the tensile testing, solute hydrogen concentration was measured by gas chromatography thermal desorption analysis (TDA) with a thermal conductivity detector at a heating rate of 100 K/h. A cylindrical sample with a 5 mm height was cut from the uniformly deformed part of the fractured specimen for TDA. The measured hydrogen concentration in the charged specimen was 133 mass ppm, which was significantly greater than the concentration of 5 mass ppm in the non-charged condition. Since the hydrogen charging was completed before the tensile tests, we consider that the hydrogen content in the specimen is nearly constant during the tensile test. The central sections of cylindrical-shaped samples cut along the tensile axis were used for microstructural characterization to avoid surface effects associated with deformation constraints. Accordingly, the analyzed dipole structures correspond to dislocation configurations formed in bulk grains. These structures were investigated in tensile deformed samples to a true strain, ε, of 0.15, which corresponds to the Stage III strain-hardening, by scanning transmission microscopy (STEM) in a JEOL JEM2800 TEM operating at 200 kV. Before imaging, the STEM samples were plasma-cleaned using an XEI Evactron 25 (XEI Scientific, Inc., Redwood City, USA) decontaminator. STEM samples were fabricated from regions of bulk grains located in the central sections of the sample gauge by using the in-situ focused ion beam (FIB) lift-out method on a Scios 2 ThermoFisher Scientific dual-beam scanning electron microscope (SEM) system at an acceleration voltage of 30 kV and a Ga^+ current of ~1000 pA on both sides of the foil followed by a final thinning procedure at 5 kV and 200 pA [18]. The size of the STEM lamella fabricated by FIB was about 20 μm × 20 μm × 100 nm. Bright-field scanning transmission microscopy (BF-STEM) images were obtained under two-beam conditions at a camera length of 8 cm and a collection angle range of 0–11 mrad. The specimens were tilted using a double-tilt sample holder for both TEM and STEM modes to satisfy either the systematic excitation condition or the two-beam excitation condition that is appropriate for observing dislocations [19]. There are invisible or blurred dislocations that satisfy $\boldsymbol{g} \bullet \boldsymbol{b} = 0$, where $\boldsymbol{g}$ and $\boldsymbol{b}$ denote the diffraction vector and Burgers vector, respectively. STEM images of dipole structures formed in the hydrogen-charged sample were taken at the beginning and end of STEM sessions to study potential damage induced by the electron beam on the dipole structures. The STEM images do not reveal any visible impact of the electron beam on the dipole structures. The measured dipole heights remain within the statistical range.

3. Results and discussion

3.1. Dipole structure

Fig. 1 shows BF-STEM images of the dislocation dipole structure formed in the hydrogen-charged (a, b) and uncharged (c, d) conditions of the Fe–19Ni–24Cr austenitic steel tensile deformed to a true strain, ε, of 0.15. The BF-STEM images were taken under two-beam conditions using a diffraction vector of $g = (1\,1\,\bar{1})$. The dislocation dipoles were mainly observed in the interior of slip bands (SBs) characterized by a high dislocation density. Examples of the SB structure are shown in Fig. 1(a–c). The analyzed grain orientations were close to [1 1 1]//TA directions (TA: tensile axis). In particular, the dipoles shown in Fig. 1(b, d) correspond to grains oriented close to the [8 8 9]//TA (hydrogen-charged) and [11 12 13]//TA (uncharged) directions, respectively. They are associated with the activation of the slip systems (1 1 0) [1 -1 1], (0–1 -1) [1 -1 1], (1 0 1) [−1 1 1], and (−1 -1 0) [−1 1 1]. According to the dipole line length, two types of dipoles can be distinguished: long dipoles (LD), with dipole line lengths ranging between 200 and 500 nm, and short dipoles (SD), with dipole line lengths < 100 nm. Short dipoles correspond to a low-energy dipole configuration [20].

The total dipole character (θ) of about 150 dipoles per condition was analyzed by the method shown in Fig. 2(a). θ is defined as the angle between the dipole line and the Burgers vector directions of the activated [−1 1 1] and [1 -1 1] slip systems that are visible under the diffraction conditions used to form the corresponding BF-STEM image. The diffraction conditions were selected as those forming images of dipole lines with strong contrast. In this imaging mode, the dissociated dipole structure is considered, as a strong diffraction contrast is formed when $| g \cdot b_p | \sim 1$ (g: diffraction vector; b_p: Burgers vector of a partial dislocation). For instance, in the example of Fig. 2(a), taking $g = (1\,1\,\text{-}1)$, $b = 1/2\,(1\,1\,0)$, $b_p = 1/6\,(2\,1\,\text{-}1)$ and $1/6\,(1\,2\,1)$, we obtain $| g \cdot b_p | = 2/3$ and 1/3. Under these diffraction conditions, the slip systems (1 1 0) [1 -1 1], and (−1 -1 0) [−1 1 1] are visible. In this case, the estimated angle between the dipole line directions and the (1 1 0) direction ranges between 12° and 90°. Fig. 2(b) shows the distributions of the dipole character measured on the uncharged and hydrogen-charged samples. The quantitative analysis indicates that the dipole structure in both conditions consists of a distribution of close-to-screw (θ: 0–20°), mixed (θ: 20–60°), and close-to-edge (θ: 60−75°) dipoles. The dipole character distribution is similar in both conditions: 7–12 % of close-to-screw,

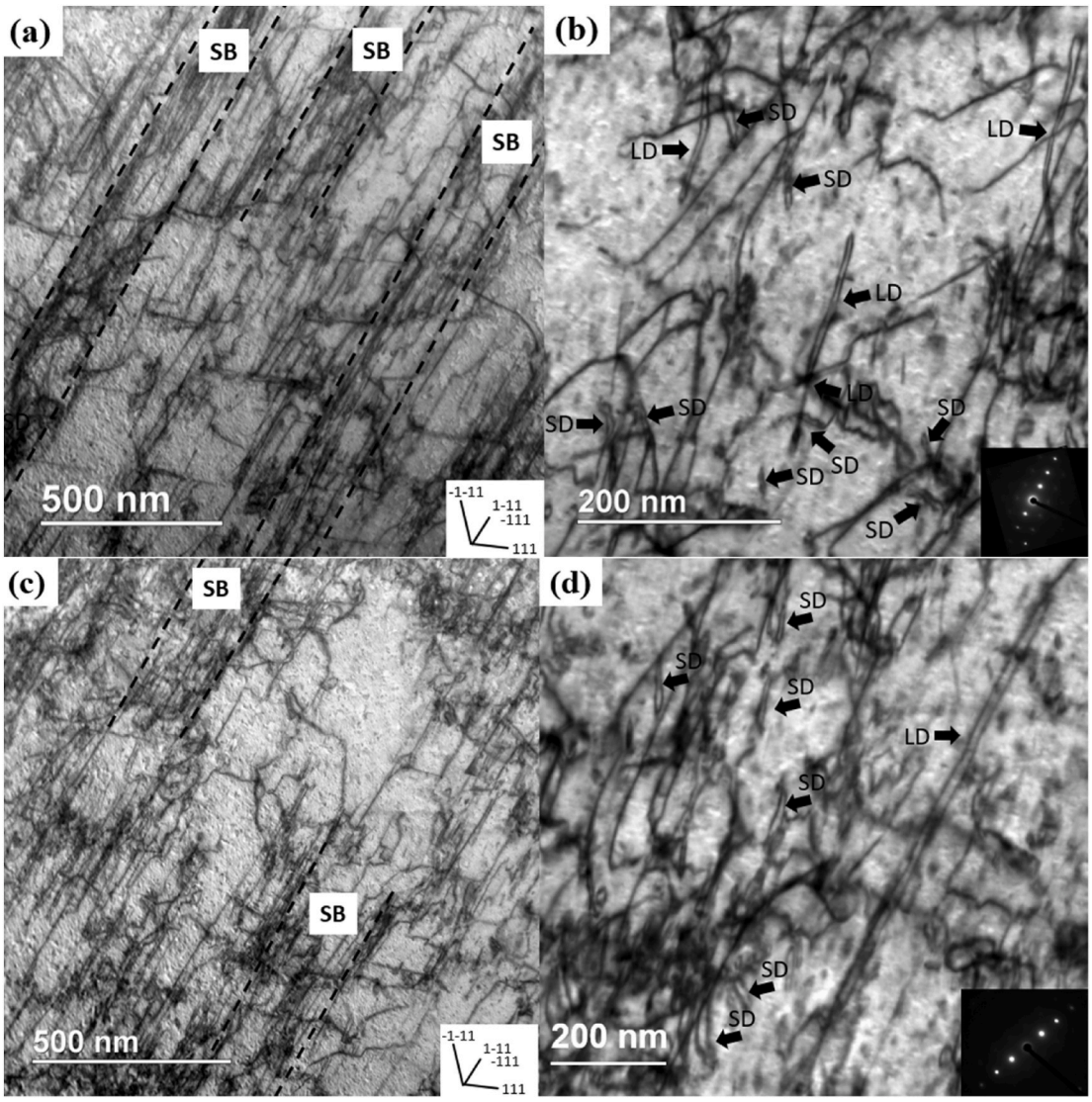

Fig. 1. BF-STEM images of the dipole structure in the hydrogen-charged (a, b) and uncharged (c, d) conditions of a Fe–19Ni–24Cr (wt. %) steel deformed to $\varepsilon = 0.15$. (a, c): Slip band (SB) structure; (b, d): Dipole structure in the interior of SBs. SD: short dipole; LD: Long dipole.

85–90 % of mixed dipoles, and a few close-to-edge dipoles (< 3 %). This analysis indicates that hydrogen does not modify the dipole character distribution.

The quantitative analysis of the dipole character reveals that SD dipoles are mainly close-to-edge-type. They exhibit zigzag shapes, which are associated with instabilities in the dislocation elastic field [21,22]. On the other hand, LD dipoles correspond to close-to-screw and mixed types. Dipole formation has been ascribed to several dislocation-based processes [23–25]. Under tensile deformation conditions, edge dipoles are mainly formed by the gliding of screw dislocations controlled by localized cross-slip (jog-dragging mechanism [23,24]). On the other hand, screw and mixed dipoles are formed by the jog-dragging of edge dislocations and the interaction of screw dislocations on non-coplanar slip systems, assisted by double cross-slip [25]. Considering that edge dislocations dominate plasticity upon the tensile deformation of fcc metals [20,26], the high population of mixed-type dipoles observed in this study can be mainly ascribed to the jog-dragging of edge dislocations.

The dipole height, h, was measured on BF-STEM images of dipoles by the method shown in Fig. 3. Fig. 3(b) shows an example of the evolution of the dislocation contrast intensity, I_{dc}, profile measured across a screw-type dipole ($\theta = 12°$) formed in the uncharged sample. The plot reveals that I_{dc} exhibits a modulated behavior, which is associated with the dislocation configuration of the dipole (depicted in the inlay of Fig. 3 (b)). In the present medium stacking fault energy material ($\gamma_{SFE} = 35$–45 mJ/m^2 [27–30]), the dipole structure is formed by two parallel dissociated dislocations. These dislocations bound stacking fault ribbons of widths d_1 and d_2, respectively. Under the current bright-field imaging conditions, these parallel dissociated dislocations produce the first and third modulation observed in the I_{dc} profile [19]. The dipole height, h, is defined as the spacing between the trailing partial of the first dissociated dislocation with Burgers vector b_{p2} and the leading partial of the second dissociated dislocation with Burgers vector b_{p3}. Accordingly, h is determined as the width of the second modulation of the I_{dc} profile. The dipole heights estimated from the analysis of the I_{dc} profile were corrected by considering the inclination angle of the corresponding [9] dipole plane with respect to the normal of the imaged section [31,32]. It is worth noting that the microscopy approach used for the dipole height measurement depends on the imaging conditions and the accurate determination of the projected geometry of the imaged dipole. Provided that the sample thickness is in the range 100–150 nm to avoid attenuation of the diffracted beam [33], the main controlling imaging parameters of the present approach are the diffraction conditions used to form the image of the dipole and the accurate determination of the

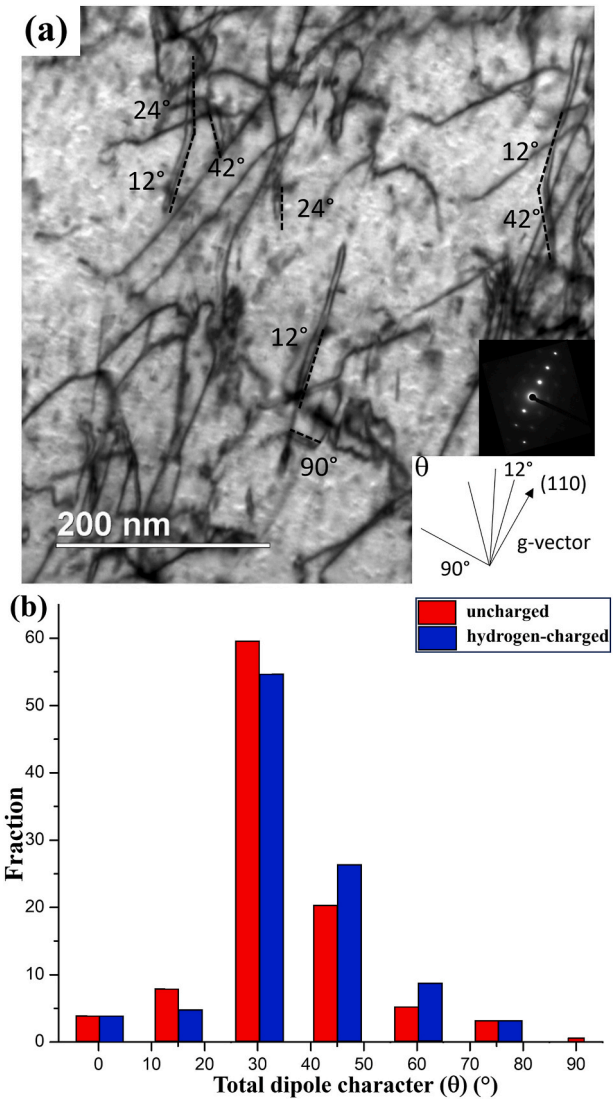

Fig. 2. (a): Analysis of the total dipole character (θ) by BF-STEM. (b): Experimental distributions of total dipole character (θ) measured in the uncharged (red bars) and hydrogen-charged (blue bars) samples of a Fe–19Ni–24Cr (wt. %) steel deformed to $\varepsilon = 0.15$. (For interpretation of the references to colour in this figure legend, the reader is referred to the Web version of this article.)

projection geometry of the imaged dipole. The optimum diffraction conditions for forming sharp BF-STEM images of a dislocation dipole correspond to two-beam conditions using a strong diffraction vector, such as (1 1 1)-type. Two-beam conditions avoid the overlapping contrast formed in multi-beam diffraction conditions, which leads to the blurring of the strain field and underestimation of the dipole height. The accurate determination of the projection geometry of the imaged dipole is key to calculating the dipole height. For this, the determination of the normal direction of the sample, the tilting angle, and the slip plane is needed.

Fig. 4 shows the dipole height distributions measured in the uncharged (red bars) and hydrogen-charged (blue bars) conditions. The dipole character range is plotted in the figure. The average dipole heights for the analyzed dipole character range are shown in Table 1. Similar to dissociated dislocations, the plot indicates that h increases with the dipole character. We consider $\theta = 0$–15° as screw-type dipoles. From the analysis, we obtain for the uncharged condition: $< h_{screw} > = 3.0 \pm 0.2$ nm, $< h_{\theta=15-30^\circ} > = 4.6 \pm 0.4$ nm, $< h_{\theta=30-60^\circ} > = 7.9 \pm 0.9$ nm, and $< h_{\theta=60-75^\circ} > = 12.1 \pm 1.0$ nm. The minimum dipole height, h_{min}, is 2.8 ± 0.2 nm. For the hydrogen-charged condition: $< h^H_{screw} > = 3.2 \pm 0.2$ nm, $< h^H_{\theta=15-30^\circ} > = 4.9 \pm 0.4$ nm, $< h^H_{\theta=30-60^\circ} > = 8.0 \pm 0.9$ nm, $< h^H_{\theta=60-75^\circ} > = 12.2 \pm 1.0$ nm, and $h^H_{\min} = 3.0 \pm 0.2$ nm. Hereinafter, the superscript H refers to the hydrogen-charged condition. These findings indicate that hydrogen slightly increases the average dipole height of screw dipoles. However, it has a negligible effect on the dipole height of close-to-edge-type dipoles. The influence of these effects on the stacking fault energy (γ_{SFE}) is analyzed in Section 3.2. These findings suggest that the impact of hydrogen on the dissociated dislocation structure depends on the dislocation character. This result agrees with recent atomic calculations on the structure of edge dissociated dipoles in hydrogen-charged Ni [4]. This study has shown that the influence of hydrogen on edge dissociated dislocations (reduction in the dissociation distance) is opposite to that reported on screw dissociated dislocations (increase in the dissociation distance).

3.2. Prismatic loop structure

Prismatic loops (PLs) aligned along <1 1 2> directions were observed at the true strain level, ε, of 0.15 in both conditions, namely, hydrogen-charged, Fig. 5(a), and uncharged, Fig. 5(b). In the uncharged condition, PL formation is mainly associated with the gliding of screw dislocations [20]. The addition of hydrogen can further promote the formation of narrow prismatic loops possibly *via* the climb of jogs assisted by hydrogen-induced vacancies, increasing their population [4]. This point will be analyzed in a future study. In this work, we have analyzed the impact of hydrogen on the average PL size at the current deformation condition. We measured the size of about 100 PLs formed in grains oriented close to the [1 1 1]//TA directions in both conditions by the analysis of the intensity contrast profile measured across a PL, as in Fig. 3. The true PL size was estimated from the PL size measured on STEM images by considering the inclination of {1 1 1} planes with respect to the imaged plane (we assumed that PLs lie on {1 1 1} planes as they are associated with the gliding of screw dislocations [20]). We obtained an average PL size of 9.3 ± 1.0 nm in the uncharged sample and 9.7 ± 1.0 nm in the hydrogen-charged sample. These values are close to the average size of Frank loops formed in austenitic steels (~9.2 nm in a Fe–12Ni–17Cr austenitic steel [34]). These results indicate that hydrogen slightly increases the average PL size, which agrees with the behavior of Frank loops formed in austenitic steels under neutron-irradiation conditions [34]. At undeformed conditions, several mechanisms for loop growth have been proposed [35–37]. These models are associated with the absorption of vacancies emitted from jogs and shrinking loops that migrate by bulk and pipe diffusion processes. The addition of solute hydrogen enhances the formation of vacancy-hydrogen clusters that can contribute to loop formation and coarsening processes [38]. Furthermore, upon straining, dislocation-loop interactions can also modify the shape and size of loops [39]. Dislocation dipoles and loops contribute to strain-hardening by reducing the dislocation mean free path by acting as additional obstacles to the primary slip system [1,2]. As suggested by Fourie and Murphy [2], the contribution of these crystal defects is proportional to their density. The addition of hydrogen can further promote the formation of narrow prismatic loops via the climb of jogs assisted by hydrogen-induced vacancies [4], increasing their population. Accordingly, hydrogen can promote the contribution of dislocation loops to the strain-hardening by increasing their population. This point will be analyzed in a further study.

3.3. Analysis of the influence of hydrogen on stacking fault energy

In this section, we estimate the influence of hydrogen on γ_{SFE} by the analysis of the dislocation configuration of the dipole structure. Following Section 3.1, we consider that the dipole structure is formed by two parallel dissociated dislocations bounding stacking fault ribbons of widths d_1 and d_2, respectively (Fig. 6(a)). The SF ribbon width (d) which

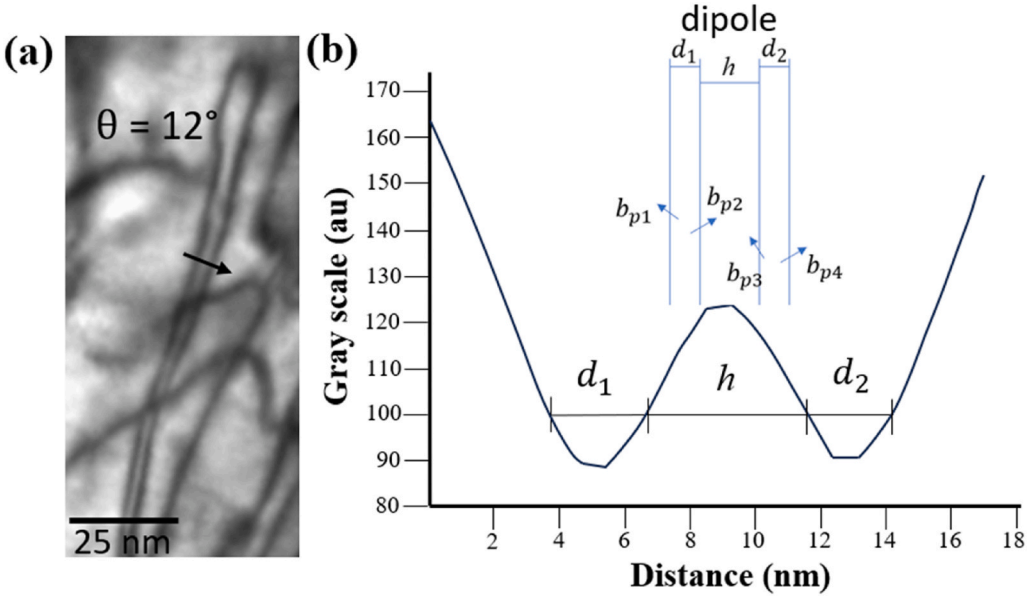

Fig. 3. Analysis method for the determination of the dipole height (h) on BF-STEM images of the dipole structure.

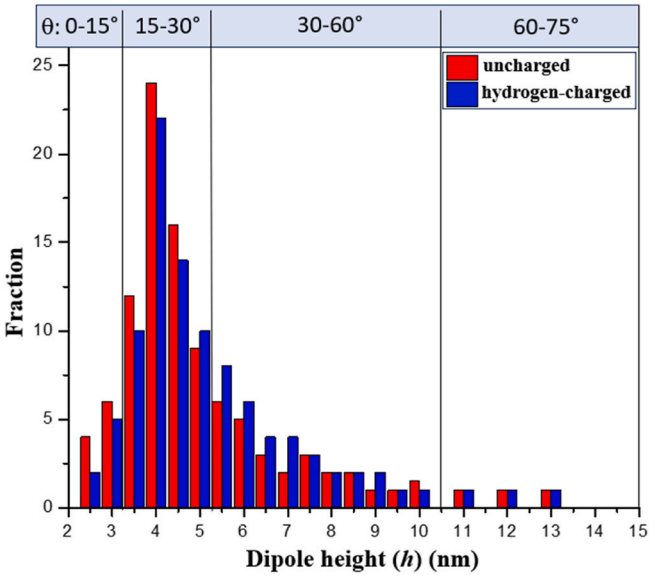

Fig. 4. Experimental dipole height (h) distributions measured in the uncharged (red bars) and hydrogen-charged (blue bars) samples of a Fe–19Ni–24Cr (wt. %) steel deformed to $\varepsilon = 0.15$. The dependence of the h distribution with total dipole character (θ) is also shown. (For interpretation of the references to colour in this figure legend, the reader is referred to the Web version of this article.)

is the distance between the two partials, is determined by the net resolved shear stress acting on each partial dislocation. In this context, we have to consider the following. The estimated discrepancy in the partial dislocation spacing (Δd) associated with a variation in the total dislocation character ($\Delta\alpha$) of a few degrees in screw-type dipoles ($\alpha <$ 10°) is smaller than the experimental spatial resolution measured on STEM images (the stacking fault energy was estimated using the minimum dipole height measured on screw-type dipoles with $\alpha \sim 5°$). Specifically, from the calculated variation of the partial dislocation spacing (d) with the total dislocation character angle (α) shown in Fig. 6(b), we estimate $\Delta d = 0.03$–0.05 nm for a variation of 5° in the total dislocation character of screw-type dipoles ($\alpha < 10°$). This value is smaller than the experimental spatial resolution of 0.2 nm measured on STEM images. Accordingly, we assume that the SF ribbon widths of the two parallel dissociated dislocations are the same, $d_1 = d_2$. Considering the anisotropic elastic theory, in the equilibrium state, the spacing between two partial dislocations (d) is given by [40]:

$$d = \frac{G_{eff} b_p^2}{8\pi\,\gamma_{SFE}} \frac{2-\nu_{eff}}{1-\nu_{eff}} \left(1 - \frac{2\nu_{eff}\cos 2\alpha}{2-\nu_{eff}}\right) \quad (1)$$

where b_p is the partial dislocation Burgers vector, γ_{SFE} is the stacking fault energy, G_{eff} is the effective shear modulus, ν_{eff} is the effective Poisson ratio, and α is the total dislocation character angle. The effective shear modulus (G_{eff}) is given by:

$$G_{eff} = \left(C_{44}\frac{(C_{11}-C_{12})}{2}\right)^{0.5} \quad (2)$$

and the effective Poisson ratio (ν_{eff}) is given by:

$$\frac{1}{1-\nu_{eff}} = \frac{1}{3G_{eff}}(C+C_{12})\left[\frac{C_{44}(C-C_{12})}{C_{11}(C+C_{12}+2C_{44})}\right]^{0.5}\left(1+2\frac{C_{11}}{C}\right) \quad (3)$$

where $C = \left[\frac{1}{2}C_{11}(C_{11}+C_{12}+2C_{44})\right]^{0.5}$. C_{11}, C_{12}, and C_{44} are the elastic stiffness constants. Eqn 1 provides a sound estimation of γ_{SFE} in anisotropic austenitic steels [13]. Using the elastic stiffness constants

Table 1
Experimental values of minimum dipole height, h_{min}, average dipole height of screw-type dipoles, $< h_{screw} >$, average dipole height of mixed-type dipoles $< h_{\theta=15-30^\circ} >$ and $< h_{\theta=30-60^\circ} >$, and the average dipole height of close-to-edge-type dipoles $< h_{\theta=60-75^\circ} >$ in the uncharged and hydrogen-charged conditions of a Fe–19Ni–24Cr (wt. %) steel deformed to $\varepsilon = 0.15$.

Condition	h_{min}	$< h_{screw} >$	$< h_{\theta=15-30^\circ} >$	$< h_{\theta=30-60^\circ} >$	$< h_{\theta=60-75^\circ} >$
Uncharged	2.8 ± 0.2	3.0 ± 0.2	4.6 ± 0.4	7.9 ± 0.9	12.1 ± 1.0
Hydrogen-charged	3.0 ± 0.2	3.2 ± 0.2	4.9 ± 0.4	8.0 ± 0.9	12.2 ± 1.0

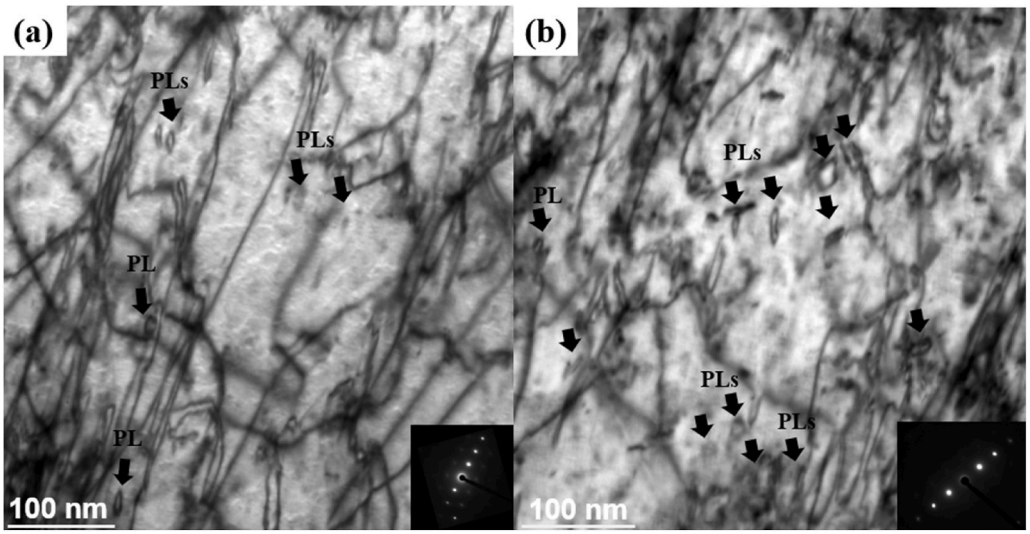

Fig. 5. BF-STEM images of prismatic loops (PLs) aligned along <1 1 2> directions formed in a Fe–19Ni–24Cr (wt. %) steel deformed to $\varepsilon = 0.15$. (a): hydrogen charged; (b): uncharged.

reported for Fe–19Ni–24Cr steel ($C_{11} = 191$ GPa, $C_{12} = 119$ GPa, and $C_{44} = 124$ GPa [41]), we obtain $G_{eff} = 67$ GPa and $\nu_{eff} = 0.38$. We calculated the theoretical dependences of the partial dislocation spacing (d) with the total dislocation character angle (α) for the lower and upper values of γ_{SFE} reported for the Fe–19Ni–24Cr steel (35 and 45 mJ/m^2 [27–30]), Fig. 6(b). These values were estimated from Eqn 1 after taking $b_p = 0.15$ nm [42] and the parameters G_{eff} (Eqn 2) and ν_{eff} (Eqn 3) estimated in this study. The plot indicates that for the Fe–19Ni–24Cr steel, d varies from 1.9 to 2.4 nm for close-to-screw to 5.0–6.6 nm for close-to-edge partials. In particular, the predicted variation of d for screw dislocations ($\alpha = 0°$), d_{screw}, with γ_{SFE} is plotted in Fig. 6(c).

Considering that the dislocation configuration of a dipole consists of two parallel dissociated dislocations [43], in the equilibrium state, the spacing between two screw partial dislocations (d) is given by [20]:

$$d = \frac{G_{eff}\, b_p^2}{2\pi\, \gamma_{SFE}} \left(1 - 2\left(\frac{d^2}{d^2 + h^2}\right)\right) \tag{4}$$

This relation takes into account the attractive interaction between the screw dissociated dislocations, both with antiparallel Burgers vector with regard to the former pair. Using Eqn 4, we can calculate the relation between d and h for a certain γ_{SFE}. Taking into account the estimated dependence of d with α calculated for the Fe–19Ni–24Cr steel (Fig. 6(b)), and assuming that the total dislocation character of each dissociated dislocation forming the dipole is the same as the dipole character, i.e., $\theta = \alpha$, we have calculated the variation of the dipole height (h) with θ for $\gamma_{SFE} = 35$, 40 and 45 mJ/m^2, Fig. 7. Only close-to-screw ($\theta < 15°$) and mixed dipoles are considered (θ: $15 - 45°$). The experimental values of h determined from the analysis of the dipole structure by STEM (Fig. 4) are also plotted (labelled as "exp-uncharged" for the uncharged condition and "exp-charged" for the hydrogen-charged condition). It can be seen that the experimental values of h are within the range of predicted values of h for $\gamma_{SFE} = 35$–45 mJ/m^2. Interestingly, the plot indicates that the values of h measured in the hydrogen-charged condition are associated with a smaller γ_{SFE} than those of the uncharged condition. This point is quantitatively analyzed as follows.

Using Eqn 4 and taking the calculated values of d_{screw} for the γ_{SFE} range of 35–45 mJ/m^2 (Fig. 6(c)), we can estimate the dependence of the minimum dipole height (h_{min}) with γ_{SFE}. In our recent study [42], we have measured the influence of solute hydrogen (139 mass ppm) on the evolution of the lattice strain components ε^{111}, ε^{220}, ε^{311}, and ε^{200} with true stress by in-situ neutron diffraction for the present Fe-19Ni-24Cr steel. In the elastic regime, five stress states were measured. Our data revealed a negligible influence of hydrogen on the lattice strain. These results indicate that hydrogen has a small effect on the elastic stiffness constants during the elastic regime. Accordingly, we can assume $G_{eff}^H = G_{eff}$. On the other hand, several studies [44–47] have shown that hydrogen can reduce the shear modulus of pure metals and alloys by about 10–20 %. This effect is associated with a reduction of the critical shear stress required for the onset of homogeneous dislocation nucleation [44,46]. Recently, DFT calculations in binary bcc FeNi and FeCr systems have estimated that 1 at. % of solute hydrogen reduces the shear modulus by about 1.3 % [48]. Considering that in the present study the hydrogen content is 133 mass ppm (~0.72 at. %), the predicted hydrogen-induced reduction in the shear modulus is 0.9 %, i.e., $G_{eff}^H = 0.99\, G_{eff}$. Fig. 8 shows the calculated dependence of the minimum dipole height (h_{min}) with γ_{SFE}, for $G_{eff}^H = G_{eff}$ (black dots) and $G_{eff}^H = 0.99\, G_{eff}$ (blue dots). The calculations indicate that in the uncharged condition, the experimental value $h_{min} = 2.8 \pm 0.2$ nm corresponds to $\gamma_{SFE} = 42 \pm 2$ mJ/m^2. For the hydrogen-charged condition, we obtain $\gamma_{SFE}^H = 40 \pm 2$ mJ/m^2 for $G_{eff}^H = G_{eff}$ and $\gamma_{SFE}^H = 39 \pm 2$ mJ/m^2 for $G_{eff}^H = 0.99\, G_{eff}$. From this analysis, we obtain $\gamma_{SFE}^H = 39.5 \pm 2.5$ mJ/m^2.

The present analysis indicates that hydrogen has a limited impact on γ_{SFE} of the Fe–19Ni–24Cr steel, reducing its value by ~6 %. This effect is mainly associated with hydrogen-induced increase in the spacing of screw-type dislocation partials, due to the limited influence of hydrogen on G_{eff}. Fig. 9 plots the hydrogen-induced reduction in γ_{SFE} reported in fcc materials with a hydrogen content of 0.5–1.0 at. % estimated by transmission electron microscopy (TEM) and computational studies (MD: molecular dynamics; MS: molecular statics; AC: atomic calculations). The data used in this figure is gathered in Table 2. Fig. 9 reveals a strong dependence of the hydrogen-induced reduction in γ_{SFE} on the chemical content. The effect ranges 20–35 % for pure Ni, 28 % for a Cr–Mn–Fe–Co–Ni high entropy alloy, and 5–20 % for Fe–Ni–Cr steels. Zhou et al. [9] have suggested that large reductions in γ_{SFE} are associated to the influence of local hydrogen concentrations at dislocation cores on the dissociated dislocation spacing. The analysis shown in Fig. 9 reveals that the results of the present study agrees with MD calculations performed in Fe–11Ni–19Cr and Fe–15Ni–15Cr steels with a hydrogen content of 1 at. % [9]. This result validates our approach based on anisotropic theory and highlights the outcomes from the model, such as the negligible influence of hydrogen on G_{eff}. Our findings are also consistent with the small influence of hydrogen on γ_{SFE} estimated by in situ neutron diffraction in the same steel containing 139 mass ppm of

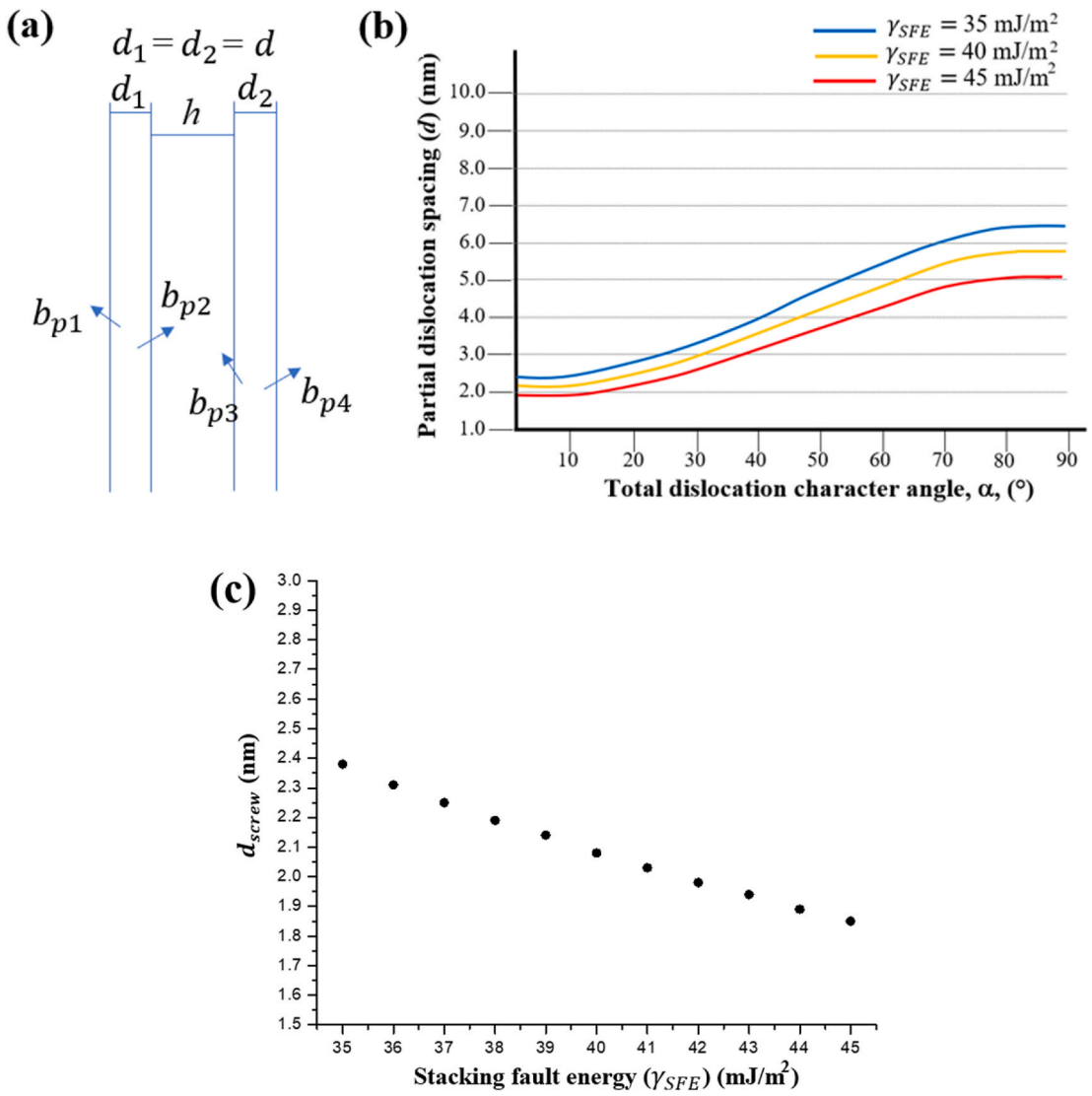

Fig. 6. (a): Schematic of the dislocation configuration of a dissociated dipole. b_p: partial dislocation Burgers vector. d_1, d_2, and d: stacking fault ribbon widths; (b): Calculated dependences (Eqn 1) of the partial dislocation spacing, d, with the total dislocation character, α, for the lower and upper values of γ_{SFE} of the Fe–19Ni–24Cr steel (35 and 45 mJ/m^2); (c): Estimated variation of d_{screw} with γ_{SFE}.

solute hydrogen [42].

Interestingly, the results obtained in this study are in contradiction with the reduction of 20–28 % measured by TEM approaches reported in the same Fe–Ni–Cr steel as that analyzed in this study and a Cr–Mn–Fe–Co–Ni fcc alloy [11,12]. It is worth comparing the main experimental and methodological characteristics of the present study to those of the former experimental works to underline the relevance of the present results. The hydrogen-charging method selected in this study (gaseous hydrogen pre-charging at high pressure and temperature) allows the controlled addition of a uniform solute hydrogen distribution in the sample gauge [17], which is a significant advance compared to former reports. In these studies, the measurement of hydrogen content was either lacking [11] or questionable [12], due to effects associated with the charging method used in that study (electrochemical charging) that influence the hydrogen diffusion rate [10]. Besides, multicomponent fcc alloys, such as austenitic alloys, are anisotropic materials. The elastic anisotropy ratio (A) of the present Fe–19Ni–24Cr steel is relatively high ($A = 2\,C_{44}/(C_{11}- C_{12}) = 3.4$), which influences the values of the elastic stiffness constants and Poisson's ratio used to determine the distance between partials. As shown in Ref. [13], the isotropic dislocation theory can overestimate γ_{SFE} by ~ 10 % and produces a larger uncertainty. It is important to note that these errors are in the range of the hydrogen-induced reduction in γ_{SFE} predicted by computational studies for a hydrogen content of 0.5–1.0 at. % (Fig. 9). The present study is the first experimental estimation of the influence of hydrogen on γ_{SFE} using anisotropic dislocation theory in an austenitic steel with an accurate content of solute hydrogen. These aspects are essential for a sound experimental evaluation of the impact of hydrogen on γ_{SFE}, which is critical to validate the predicted values calculated by computational methods.

3.4. *Influence of hydrogen-induced reduction in the stacking fault energy on deformation behavior*

In this section, we evaluate the impact of the present findings on the deformation behavior of the Fe–19Ni–24Cr steel. According to the classical Friedel-Escaig mechanism for cross-slip of a single screw dislocation, the energy barrier for cross-slip inversely scales with γ_{SFE} [49]. This relation has been used to evaluate the effect of hydrogen on the cross-slip activity in fcc materials. However, recent atomistic calculations by Curtin's group have indicated that the activation energy for cross-slip in fcc solid solutions is dominated by random solute

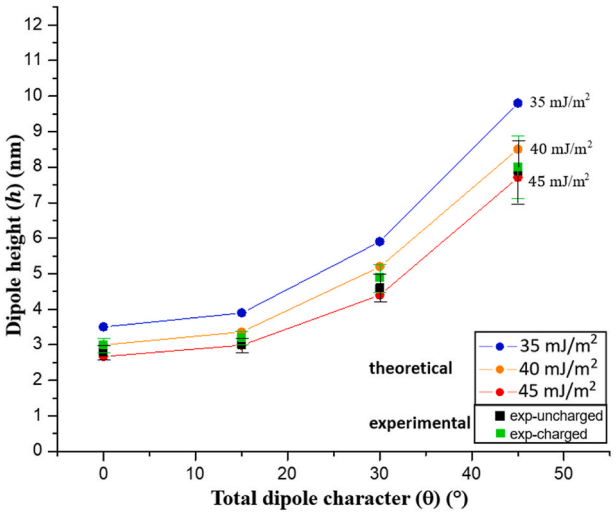

Fig. 7. Estimated variation of the dipole height (h) with dipole character (θ) for γ_{SFE} = 35, 40, and 45 mJ/m^2 (labelled as "theoretical"). The experimental h values estimated by the analysis of the dipole structure by STEM are also plotted (labelled as "exp-uncharged" and "exp-charged").

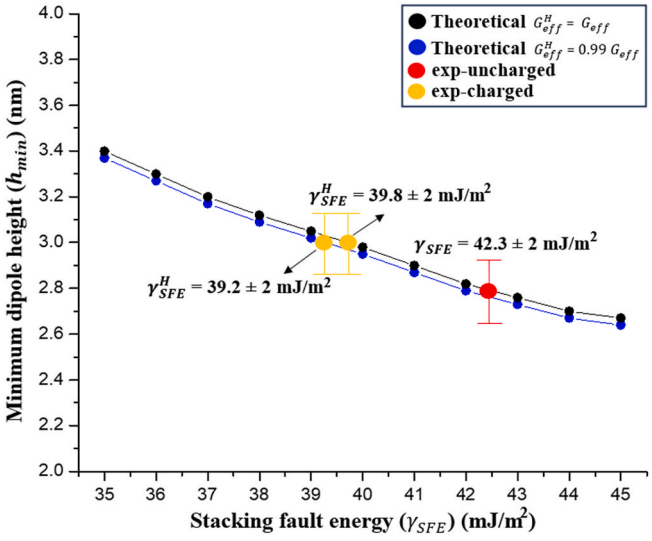

Fig. 8. Estimated variation of the minimum dipole height (h_{min}) with stacking fault energy (γ_{SFE}) for $G^H_{eff} = G_{eff}$ (black dots) and $G^H_{eff} = 0.99\ G_{eff}$ (red dots). The experimental h_{min} values obtained by the analysis of the dipole structure by STEM are also plotted (labelled as "exp-uncharged" and "exp-charged"). The estimated γ_{SFE} and γ^H_{SFE} corresponding to the experimental h_{min} are shown in the plot. The superscript H refers to the hydrogen-charged condition. (For interpretation of the references to colour in this figure legend, the reader is referred to the Web version of this article.)

fluctuations, i.e., it is a stochastic variable [50,51]. These studies suggest that average material parameters, such as normalized stacking fault energy (γ_{SFE}/Gb), can not provide valuable insight into the activation of cross-slip in fcc solid solutions, such as the present Fe–19Ni–24Cr steel. Interestingly, molecular dynamic calculations performed in a Fe–11Ni–19Cr steel have indicated that hydrogen additions in the range of the present study (0.5–1.0 at. %) increase the energy barrier for cross-slip by a factor of 2, enabling planar slip localization [52]. This effect can assist in the activation of damage mechanisms, resulting in hydrogen embrittlement (HE) [10,53]. This process is evaluated in detail by the analysis of fracture behavior and characterization of the dislocation structure in an ongoing study [54].

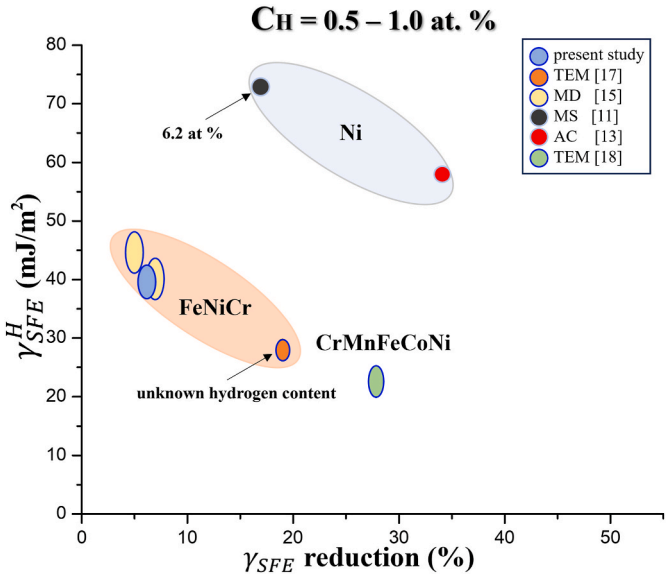

Fig. 9. Reported influence of hydrogen content (C_H) of 0.5–1.0 at. % on stacking fault energy (γ_{SFE}) of several fcc materials (Fe–Ni–Cr steels, a Cr–Mn–Fe–Co–Ni, and Ni). The results of the present study for the Fe–19Ni–24Cr steel are also shown. The data are from Table 2. MD: molecular dynamics; MS: molecular statics; AC: atomic calculations; TEM: transmission electron microscopy.

The increase in the energy barrier for cross-slip can also influence the deformation behavior by limiting the formation of dislocation structures controlled by cross-slip, such as dislocation cells [55,56]. Fig. 10 shows electron channeling contrast (ECC) images of the dislocation configuration formed at ε = 0.15 in grains oriented close to [0 0 1]//TA directions in the uncharged (a) and hydrogen-charged conditions (b). The ECC images reveal the formation of dislocation cells in both conditions. This finding indicates that the addition of 133 mass ppm of solute hydrogen does not suppress dislocation cell formation in the Fe–19Ni–24Cr steel. Our former study [57] has shown that in a Fe-30.5Mn-2.1Al-1.2C (wt. %) austenitic steel, the reduced cross-slip activity associated with the effect of carbon solute on the constriction energy for cross-slip promotes the formation of Taylor lattices instead of dislocation cells in grains oriented close to [0 0 1]//tensile axis. In the present study, a hydrogen content of 133 mass ppm does not inhibit dislocation cell formation, suggesting that the reduced cross-slip activity has a minor effect on dislocation cell formation. The impact of this result on the deformation behavior is analyzed in an ongoing study [54].

4. Conclusions

We quantitatively evaluated the influence of uniform distribution of solute hydrogen (133 mass ppm) on dislocation dipole and loop structures in a Fe–19Ni–24Cr austenitic steel by an approach based on scanning transmission electron microscopy (STEM) and anisotropic dislocation theory. Statistical analyses of prismatic loop size and dipole height were performed with sufficient statistical significance using an imaging approach that analyzes the intensity contrast profile across crystal defects on STEM images, considering the projection geometry of the imaged defect. The dissociated dipole structure was examined by a model based on anisotropic dislocation theory that allows the estimation of the stacking fault energy with greater accuracy than approaches used in the literature. The following conclusion can be drawn:

- Hydrogen addition leads to several effects on crystallographic defects, increasing the average prismatic loop size and average dipole height of screw-type dipoles.

Table 2
Reported influence of hydrogen (0.5–1.0 at. %) on the stacking fault energy (γ_{SFE}) of fcc materials. MD: molecular dynamics; MS: molecular statics; AC: atomic calculations; TEM: transmission electron microscopy; STEM: scanning transmission microscopy.

Material	γ_{SFE} (mJ/m^2)	γ^{H}_{SFE} (mJ/m^2)	γ_{SFE} reduction	Technique	Hydrogen content (at ppm)	Reference
Fe19Ni24Cr	42 ± 2	39.5 ± 2	7 %	STEM	7300	Present study
Fe15Ni15Cr	48 ± 3	45 ± 3	5 %	MD	10000	[9]
Fe11Ni19Cr	44 ± 3	41 ± 3	7 %	MD	10000	[9]
Ni	88	73	17 %	MS	62000	[5]
Fe19Ni24Cr	35 ± 1	28 ± 1	19 %	TEM	Unknown	[11]
CrMnFeCoNi	31.5 ± 3.5	22.5 ± 2.5	29 %	TEM	6300	[12]
Ni	88	58	34 %	AC	5000	[7]

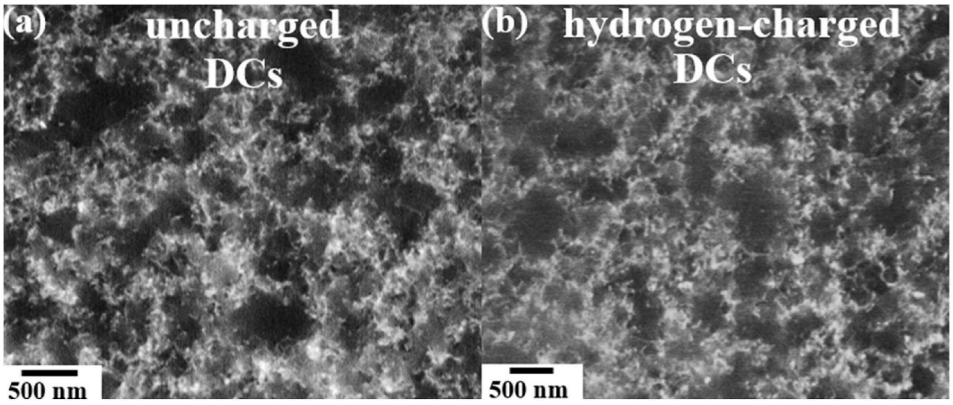

Fig. 10. Electron channeling contrast (ECC) images of the dislocation cell structure formed in grains oriented close to [0 0 1]//tensile axis directions in the uncharged (a) and hydrogen-charged (b) conditions of a Fe–19Ni–24Cr (wt. %) steel deformed to $\varepsilon = 0.15$.

- The analysis of the dissociated dipole structure indicates that a hydrogen content of 133 mass ppm (~0.7 at. %) reduces the stacking fault energy by ~ 6 %. This effect is mainly associated with a hydrogen-induced increase in the spacing of screw-type partial dislocations, due to the negligible influence of hydrogen on the effective shear modulus.
- The hydrogen-induced reduction in the stacking fault energy does not inhibit the formation process of dislocation structures controlled by cross-slip, such as dislocation cells.

The developed experimental framework highlights the influence of hydrogen-charging conditions, imaging analysis method, and anisotropic elastic theory on the dissociated structure of dislocations, which is key to accurately determining the effect of hydrogen on stacking fault energy in fcc alloys.

CRediT authorship contribution statement

Ivan Gutierrez-Urrutia: Writing – review & editing, Writing – original draft, Investigation, Funding acquisition, Conceptualization. **Yuhei Ogawa:** Writing – review & editing. **Akinobu Shibata:** Writing – review & editing.

Declaration of competing interest

The authors declare that they have no known competing financial interests or personal relationships that could have appeared to influence the work reported in this paper.

Acknowledgments

This work was supported by JSPS KAKENHI Grant Number JP25K08261.

References

[1] Chen HS, Gilman JJ, Head AK. Dislocation multipoles and their role in strain-hardening. J Appl Phys 1964;35:2502–14. https://doi.org/10.1063/1.1702890.
[2] Fourie JT, Murphy RJ. Elongated dislocation loops and the stress-strain properties of copper single crystals. Phil Mag 1962;7:1617–31. https://doi.org/10.1080/14786436208213699.
[3] Hachet G, Oudriss A, Barnoush A, Milet R, Wan D, Metsue A, Feaugas X. The influence of hydrogen on cyclic plasticity of <001> oriented nickel single crystal. Part I: dislocation organisations and internal stresses. Int J Plast 2020;129:102611. https://doi.org/10.1016/j.ijplas.2019.09.017.
[4] Hachet G, Metsue A, Oudriss A, Feaugas X. The influence of hydrogen on cyclic plasticity of <001> oriented nickel single crystal. Part II: stability of edge dislocation dipoles. Int J Plast 2020;129:102667. https://doi.org/10.1016/j.ijplas.2020.102667.
[5] Tang Y, El-Awady JA. Atomistic simulations of the interactions of hydrogen with dislocations in fcc metals. Phys Rev B 2012;86:174102. https://doi.org/10.1103/PhysRevB.86.174102.
[6] He Y, Li Y, Zhao X, Yu H, Chen C. Effect of hydrogen atom and hydrogen filled vacancies on stacking fault energy in γ-Fe by first-principles calculations. Int J Hydrogen Energy 2019;44:17136–45. https://doi.org/10.1016/j.ijhydene.2019.04.229.
[7] Zhu Y, Zheng Z, Huang M, Liang S, Li Z. Modeling of solute hydrogen effect on various planar fault energies. Int J Hydrogen Energy 2020;45:9162–73. https://doi.org/10.1016/j.ijhydene.2020.01.107.
[8] Xie Z, Wang Y, Lu C, Dai L. Sluggish hydrogen diffusion and hydrogen decreasing stacking fault energy in a high-entropy alloy mater. Today Comm 2021;26:101902. https://doi.org/10.1016/j.mtcomm.2020.101902.
[9] Zhou XW, Nowak C, Skelton RS, Foster ME, Ronevich JA, Marchi CS, Sills RB. An fe–ni–cr–h interatomic potential and predictions of hydrogen-affected stacking fault energies in austenitic stainless steels. Int J Hydrogen Energy 2022;47:651–65. https://doi.org/10.1016/j.ijhydene.2021.09.261.
[10] Robertson IM, Birnbaum HK, Sofronis P. Hydrogen effects on plasticity. In: Hirth JP, Kubin L, editors. Dislocations in solids, 15. Elsevier Science; 2009.
[11] Ferreira PJ, Robertson IM, Birnbaum HK. Influence of hydrogen on the stacking-fault energy of an austenitic stainless steel. Mater Sci Forum 1996;207–209:93–6.
[12] Kim HJ, Min-Kyung, Kim G, Lee SY, Jo MG, Kim H, Suh JY, Lee J. Infuence of hydrogen absorption on stacking fault of energy of a face-centered cubic high entropy alloy, metals mater. Inter 2022;28:2637–45. https://doi.org/10.1007/s12540-021-01163-8.
[13] Pierce DT, Jiménez JA, Bentley J, Raabe D, Oskay C, Wittig JE. The influence of manganese content on the stacking fault and austenite/e-martensite interfacial energies in Fe–Mn–(Al–Si) steels investigated by experiment and theory. Acta Mater 2014;68:238–53. https://doi.org/10.1016/j.actamat.2014.01.001.

[14] Zhu Y, Ophus C, Toloczko MB, Edwards DJ. Towards bend-contour-free dislocation imaging via diffraction contrast STEM. Ultramicroscopy 2018;193:12–23. https://doi.org/10.1016/j.ultramic.2018.06.001.
[15] Xiu P, Bei H, Zhang Y, Wang L, Field KG. STEM characterization of dislocation loops in irradiated FCC alloys. J Nucl Mater 2021;544:152658. https://doi.org/10.1016/j.jnucmat.2020.152658.
[16] Ogawa Y, Hosoi H, Tsuzaki K, Redarce T, Takakuwa O, Matsunaga H. Hydrogen, as an alloying element, enables a greater strength-ductility balance in an Fe-Cr-Ni-based, stable austenitic stainless steel. Acta Mater 2020;199:181–92. https://doi.org/10.1016/j.actamat.2020.08.024.
[17] Nishida H, Ogawa Y, Tsuzaki K. Chemical composition dependence of the strength and ductility enhancement by solute hydrogen in Fe–Cr–Ni-based austenitic alloys. Mater Sci Eng 2022;836:142861. https://doi.org/10.1016/j.msea.2022.142681.
[18] Gutierrez-Urrutia I, Ogawa Y, Shibata A. Hydrogen-enhanced microbanding in an austenitic FeMnAlC low-density steel: effect on hydrogen embrittlement resistance. Acta Mater 2024;280:120335. https://doi.org/10.1016/j.actamat.2024.
[19] Williams DB, Carter CB. Transmission electron microscopy. A textbook for materials science. Springer; 2009.
[20] Anderson PM, Hirth JP, Lothe J. Theory of dislocations. Cambridge University Press; 2017.
[21] Clarebrough LM, Head AK. Unstable directions of shockley partial dislocations. Phys Stat Sol 1969;33:431–4.
[22] Carter CB. The formation and properties of faulted dipoles. Phil Mag 1977;36:147–67. https://doi.org/10.1080/00318087708244454.
[23] Johnston WG, Gilman JJ. Dislocation multiplication in lithium fluoride crystals. J Appl Phys 1960;31(4):632–43. https://doi.org/10.1063/1.1735655.
[24] Jackson PJ. Dislocation modelling of shear in F.C.C. crystals. Prog Mater Sci 1985;29:139–75. https://doi.org/10.1016/0079-6425(85)90009-X.
[25] Tetelman AS. Dislocation dipole formation in deformed crystals. Acta Metall 1962;10:813–20. https://doi.org/10.1016/0001-6160(62)90095-0.
[26] Veyssière P, Chiu Y-L. Equilibrium and passing properties of dislocation dipoles, Phil. Mag 2007;87:3351–72. https://doi.org/10.1080/14786430601021678.
[27] Rhodes CG, Thompson AW. The composition dependence of stacking fault energy in austenitic stainless steels. Metall Trans 1977;8A:1901–6.
[28] Vitos L, Korzhavyi PA, Johnasson B. Evidence of large magnetostructural effects in austenitic stainless steels. Phys Rev Lett 2006;96:117210. https://doi.org/10.1103/PhysRevLett.96.117210.
[29] Miodownik AP. The calculation of stacking fault energies in fe-ni-cr alloys. Calphad 1978;2:207–26. https://doi.org/10.1016/0364-5916(78)90010-X.
[30] Ishida K. Direct estimation of stacking fault energy by thermodynamic analysis. Phys Status Solidi A Appl Res 1976;36:717–28. https://doi.org/10.1002/pssa.2210360233.
[31] Gutierrez-Urrutia I. Quantitative analysis of electron channeling contrast of dislocations. Ultramicroscopy 2019;206:112826. https://doi.org/10.1016/j.ultramic.2019.112826.
[32] Gutierrez-Urrutia I. Analysis of electron channeling contrast of stacking faults in fcc materials. Microsc Microanal 2021;27:318–25. https://doi.org/10.1017/S1431927620024952.
[33] Reimer L, Kohl H. Transmission electron microscopy. Physics of image formation. fifth ed. Springer; 2008.
[34] Pokor C, Brechet Y, Dubuisson P, Massoud J-P, Barbu A. Irradiation damage in 304 and 316 stainless steels: experimental investigation and modeling. Part I: evolution of the microstructure. J Nucl Mater 2004;326:19–29. https://doi.org/10.1016/0001-6160(73)90050-3.
[35] Kirchner HOK. Size distribution of dislocation loops. Acta Metall 1973;21:85–91.
[36] Eyre BL, Maher DM. Neutron irradiation damage in molybdenum. II. The influence of radiation-anneal hardening on the defect structure. Phil Mag 1971;24:767–97. https://doi.org/10.1080/14786437108216394.
[37] Powell J, Burke J. A determination of the elastic energy of dislocation loops from coarsening kinetics, Phil. Mag 1975;31:943–51. https://doi.org/10.1080/14786437508229644.
[38] Hatano M, Fujinami M, Arai K, Fujii H, Nagumo M. Hydrogen embrittlement of austenitic stainless steels revealed by deformation microstructures and strain-induced creation of vacancies. Acta Mater 2014;67:342–53. https://doi.org/10.1016/j.actamat.2013.12.039.
[39] Rodney D. Molecular dynamics simulation of screw dislocations interacting with interstitial frank loops in a model FCC crystal. Acta Mater 2004;52:607–14. https://doi.org/10.1016/j.actamat.2003.09.044.
[40] Aerts E, Delavignette P, Siems R, Amelinckx S. Stacking fault energy in silicon. J Appl Phys 1962;33:3078. https://doi.org/10.1063/1.1728570.
[41] Mangalick MC, Fiore NF. Orientation dependence of dislocation damping and elastic constants in Fe-18Cr-Ni single crystals. Trans Metall Soc AIME 1968;242:2263–364.
[42] Ito T, Ogawa Y, Gon W, Mao W, Kawasaki T, Okada K, Shibata A, Harjo S. Role of solute hydrogen on mechanical property enhancement in Fe–24Cr–19Ni austenitic steel: an in situ neutron diffraction study. Acta Mater 2025;287:120767. https://doi.org/10.1016/j.actamat.2025.120767.
[43] Castillo-Rodrıguez M, Sigle W. Dislocation dissociation and stacking-fault energy calculation in strontium titanate. Scripta Mater 2010;62:270–3. https://doi.org/10.1016/j.scriptamat.2009.11.016.
[44] Nibur KA, Bahr DF, Somerday BP. Hydrogen effects on dislocation activity in austenitic stainless steel. Acta Mater 2006;54:2677–84. https://doi.org/10.1016/j.actamat.2006.02.007.
[45] Taketomi S, Matsumoto R, Miyazaki N. Atomistic study of the effect of hydrogen on dislocation emission from a mode II crack tip in alpha iron. Int J Mech Sci 2010;52:334–8. https://doi.org/10.1016/j.ijmecsci.2009.09.042.
[46] Barnoush A, Zamanzade M, Vehoff H. Direct observation of hydrogen-enhanced plasticity in super duplex stainless steel by means of in situ electrochemical methods. Scripta Mater 2010;62:242–5. https://doi.org/10.1016/j.scriptamat.2009.11.007.
[47] Lunarska E, Zielinski A, Smialowski M. Effect of hydrogen on shear modulus of polycrystalline α iron. Acta Metall 1977;25:305–8. https://doi.org/10.1016/0001-6160(77)90149-3.
[48] Shi Y, Yu X, Chen C, Yu H. Infuence of hydrogen on the elastic properties and dislocation behavior in Fe–Cr and Fe–Ni alloys by DFT calculations. Sci Rep 2024;14:21338. https://doi.org/10.1038/s41598-024-71903-4.
[49] Friedel J. Dislocations. Addison-Wesley Publishing Company Inc.; 1964.
[50] Nöhring WG, Curtin WA. Dislocation cross-slip in fcc solid solution alloys. Acta Mater 2017;128:135–48. https://doi.org/10.1016/j.actamat.2017.02.027.
[51] Nohring WG, Curtin WA. Cross-slip of long dislocations in FCC solid solutions. Acta Mater 2018;158:95–117. https://doi.org/10.1016/j.actamat.2018.05.027.
[52] Zhou ZW, Leon-Cazares FD, Marchi CS. New molecular dynamics studies of hydrogen effects on cross-slip energy barriers in austenitic stainless steels. Comput Mater Sci 2025;257:113990. https://doi.org/10.1016/j.commatsci.2025.113990.
[53] Robertson IM. The effect of hydrogen on dislocation dynamics. Eng Fract Mech 2001;68:671–92. https://doi.org/10.1016/S0013-7944(01)00011-X.
[54] I. Gutierrez-Urrutia, Y. Ogawa, A. Shibata, Submitted to Acta Mater.
[55] Kuhlmann-Wilsdorf D, Van Der Merwe JH. Theory of dislocation cell sizes in deformed metals. Mater Sci Eng, A 1982;55:79–83. https://doi.org/10.1016/0025-5416(82)90086-6.
[56] Jackson PJ, Kuhlmann-Wilsdorf D. Low-energy dislocation cell structures produced by cross-slip. Scripta Metall 1982;16:105–7. https://doi.org/10.1016/0036-9748(82)90412-4.
[57] Gutierrez-Urrutia I, Raabe D. Multistage strain hardening through dislocation substructure and twinning in a high strength and ductile weight-reduced Fe-Mn-Al-C steel. Acta Mater 2012;60:5791–802. https://doi.org/10.1016/j.actamat.2012.07.018.